

www.acsanm.org Article

Hydro-Expandable Calcium Phosphate Micro/Nano-Particles with Controllable Size and Morphology for Mechanical Ablation

Tengyu He, David G. Bradley, Jiajing Zhou, Alec Jorns, Yash Mantri, John V. Hanna, and Jesse V. Jokerst*



Cite This: https://doi.org/10.1021/acsanm.1c00285



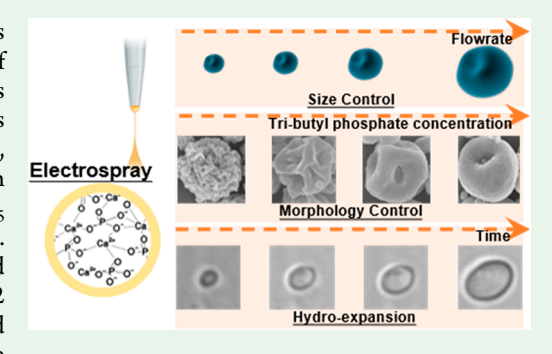
ACCESS

III Metrics & More

Article Recommendations

Supporting Information

ABSTRACT: Phosphate-based glasses are well-studied biodegradable materials in the bulk. However, less is known about the synthesis and properties of phosphate glass when prepared as microparticles or nanoparticles. These glasses have excellent biodegradability and biocompatibility. Therefore, phosphate glass micro/nanoparticles have significant potential for advances in drug delivery, bioimaging, degradable implants, and tissue engineering. In this study, calcium phosphate micro/nanoparticles (CPPs) with the composition $(P_2O_5)_{25}$ -(CaO) $_{75}$ were prepared through a combination of the sol—gel and electrospray methods. This synthesis method shows great flexibility in controlling the size and morphology of CPPs. CPPs with an average diameter in the range of 345–952 nm and various morphologies including carnation flower-like, golf-ball-like, and apple-like were obtained. Optical microscopy was further used to demonstrate



that the CPPs can have an average size increase of 95% in diameter and 720% in volume within the first 5–10 min of hydration in neutral aqueous media. The hydro-expansion process is accompanied by a two-stage ion release of phosphorus and calcium. We propose to utilize the expansion of the particle to mechanically ablate tissue and destroy cells.

KEYWORDS: electrospray, sol-gel, phosphate glasses, expansion, size, morphology, nanoparticles

■ INTRODUCTION

Bulk phosphate-based glasses have been extensively studied for decades. $^{1-14}$ This research interest is driven by three unique properties: biodegradability and biocompatibility, $^{2-11}$ tunable dissolution rate, $^{15-17}$ and ease of drug and biomolecule loading. $^{17-23}$ Different from their silicate counterparts, $^{16,24-26}$ phosphate glasses can completely dissolve in aqueous media and release ions such as Ca^{2+} and Na^+ that are routinely found in the human body. $^{2-11,15}$ This biodegradability is a direct result of the underlying chemical structure. The phosphate glass consists of an inorganic phosphate network along with modifiers such as metal oxides. The PO_4^{3-} tetrahedron unit contains at least one terminal oxygen and shares the other three with neighboring PO_4^{3-} units. This terminal oxygen reduces the connectivity of phosphate glasses compared to their silicate-based counterparts. 5

The connectivity is further reduced by adding modifier metal oxides (e.g., CaO, Na₂O, MgO, K₂O, Al₂O₃, Fe₂O₃, and TiO₂), which depolymerize the glass structure by converting the bridging oxygens into nonbridging oxygens. Second, the capability of introducing versatile modifier oxides makes the dissolution rate tunable from hours to several weeks. ¹⁶ Third, phosphate glasses can have biomedical functions: Drugs and biomolecules (e.g., trypsin inhibitor, ²¹ tetracycline, ²² growth factors, ²³ gentamicin sulfate, ¹⁹ vancomycin ¹⁷) can be easily loaded into the glass matrix and then released as the glass

dissolves. These properties make phosphate glasses promising candidates for biological applications such as bioimaging, ²⁷ drug delivery, ^{17–23} tissue engineering, ¹⁵ bone regeneration, ¹⁴ bacterial control, ¹⁵ neural repair, ^{15,28} oral healthcare, ²⁹ bioresorbable optical fiber, ⁵ etc.

Bulk phosphate glasses are typically synthesized via the meltquenching of precursors. This is a high-temperature process (~1000 °C) and incompatible with most biomolecules and drugs. More recently, sol—gel methods have been shown to create bulk phosphate glasses with a wide range of compositions below 200 °C. 11,18,30–34 In the sol—gel process, the phosphate precursors (e.g., *n*-butyl phosphate and triethyl phosphate) and desired metal oxide precursors (e.g., sodium methoxide and calcium methoxyethoxide) are mixed, hydrolyzed, and condensed to form the gel and carefully dried to form the glass.

Although bulk phosphate glasses are established, studies on the synthesis and properties of phosphate glass micro/ nanoparticles are still limited. The reduction of the size to

Received: January 28, 2021 Accepted: March 24, 2021



ACS Applied Nano Materials www.acsanm.org

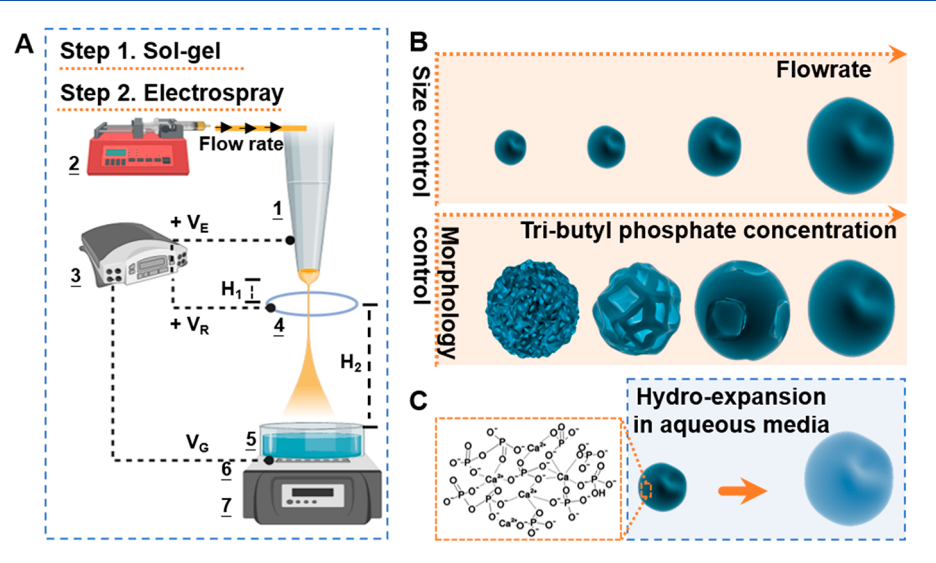


Figure 1. (A) Schematic illustration of the combined sol—gel and electrospray process. The sol solution prepared from the sol—gel chemistry (step 1) was pumped through the emitter charged with a high-voltage (step 2). This process generated fine droplets, which were collected by the heated silicone oil to form CPPs. 1, emitter; 2, syringe pump; 3, high voltage generator; 4, ring electrode; 5, silicone oil bath; 6, ground electrode; 7, hot plate. $V_{\rm E}$, the voltage of the emitter; $V_{\rm R}$, the voltage of the ring electrode; $V_{\rm G}$, the voltage of the ground electrode; $H_{\rm 1}$, the distance between the emitter and ring; $H_{\rm 2}$, the distance between the ring and ground electrode (working distance). This figure was created with BioRender.com. Main findings of this study include (B) the size and morphology control achieved by tuning the flow rate and tributyl phosphate concentration, respectively and (C) the hydro-expansion behavior of CPPs in aqueous media. Inset: schematic illustration of the phosphate glass network modified by calcium oxide. Note that this scheme does not reflect the actual chemical structure and composition.

micro/nano range may benefit biomedical applications such as drug delivery, bioimaging, and degradable implants. One approach for the preparation of nano phosphate glasses is the combined sol–gel and electrospray method. Electrospray is an electrohydrodynamic atomization process that generates small charged droplets. Micro/nano- materials with controllable size and morphology can be formed once the asgenerated droplets are further solidified. This method has been used in previous research to generate biodegradable $(P_2O_5)_{55}$ – $(CaO)_{30}$ – $(Na_2O)_{15}$ glass nanoparticles in the range of 200–500 nm. These phosphate glass nanoparticles demonstrate good biodegradability and were exploited as a transient contrast agent for ultrasound stem cell imaging. However, influences of synthetic parameters such as the solvent physical property and the electrospray voltage, flow rate, and working distance have not been explored in this work.

Here, we further refine this method to prepare $(P_2O_5)_{25}$ – $(CaO)_{75}$ calcium phosphate particles (CPPs) via a combination of sol–gel and electrospray. CPPs of the size in the range of 345–952 nm and various morphologies including carnation flower-like, golf-ball-like, and apple-like were obtained by tuning the flow rate of the electrospray process and tributyl phosphate concentration. More importantly, we also report the discovery of the hydro-expansion property of CPPs associated with the degradation process in aqueous media at pH 10 and 7. To the best of our knowledge, this is the first detailed study of size and morphology control and the first report demonstrating the hydro-expansion property of phosphate-based glass micro/nano particles. We envision that the expansion of the particle could be utilized to mechanically ablate tissue and destroy cells.

RESULTS AND DISCUSSION

Synthesis, Composition, and Structure of CPPs. CPPs were prepared with a combination of sol-gel and electrospray²⁷ (see Materials and Methods). Briefly, a sol solution was

prepared using *n*-butyl phosphate (NBP) and calcium methoxyethoxide (CME) as phosphate and calcium precursors, respectively. As-prepared sol solution was subsequently electrosprayed with the setup as shown in Figure 1A. In the electrospray, the sol solution was pumped through a metal needle and charged by the applied high voltage. As a result, fine droplets were formed and collected by the silicone oil bath maintained at 150 °C. CPPs finally formed in the silicone oil bath after solvent evaporation. The size and morphology can be well-controlled by adjusting the flow rate in the electrospray parameters and the solvent mixture of the sol (Figure 1B), which will be discussed later. A summary of the sample ID and detailed synthetic parameters including the sol–gel recipe, flow rate, voltage, and working distance are provided in Supporting Information (SI) Table S1.

Article

A comparison of the intended composition of CPPs and that determined by EDX and ICP-MS is shown in Table 1. The

Table 1. Composition of CPPs

	intended ^a		EDX^{b}		ICP-MS ^b	
sample ID	P ₂ O ₅ (mol %)	CaO (mol %)	P ₂ O ₅ (mol %)	CaO (mol %)	P ₂ O ₅ (mol %)	CaO (mol %)
CPP-4 ^c	25.0	75.0	24.6	75.4	25.1	74.9
CPP-9 ^c	25.0	75.0	25.3	74.7	26.0	74.0

"The intended value was calculated based on the ratio of NBP and CME chemical input in the sol—gel process. "Both EDX and ICP-MS results were converted to mol % for comparison. "See SI Table S1 for specific synthetic parameters.

EDX and ICP-MS results are consistent with the intended CPPs composition, $(P_2O_5)_{25}$ – $(CaO)_{75}$. Note that CPP-4 and CPP-9 were prepared without and with tributyl phosphate (TBP) addition, respectively. No significant compositional difference was found in these two samples indicating that TBP did not react with the sol. However, the addition of TBP was

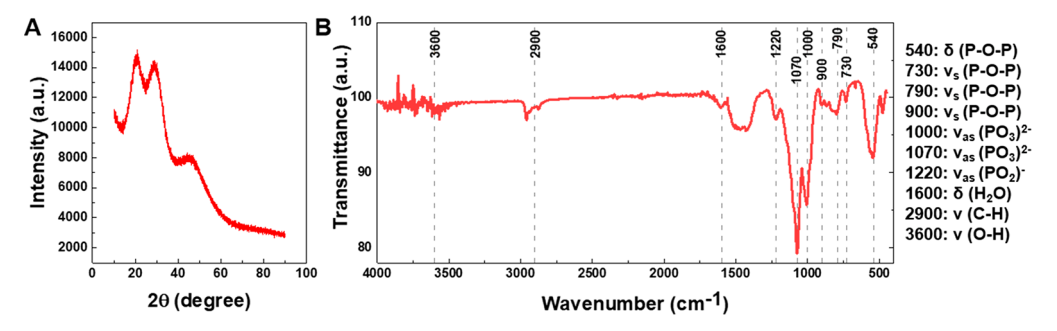


Figure 2. (A) XRD pattern of CPP-4 indicating the amorphous nature and (B) FTIR spectrum and band assignments for CPP-4 indicating the presence of P-O-P bonding and Q^1 and Q^2 species. Abbreviations: ν , stretching; δ , deformation; s, symmetric; as, asymmetric. See SI Table S1 for detailed sample ID and synthetic parameters.

found to affect the morphology of particles, which will be discussed later.

The structural characterization of the CPPs used a combination of XRD, FTIR, and ³¹P MAS NMR techniques. The XRD pattern of the as-prepared CPPs (Figure 2A) shows three broad reflections observed between 20 and 60 degrees 2θ , which indicates the amorphous nature of these particles as reported in the literature. ^{36–38} Figure 2B shows that the nature of bonding in the CPPs can be determined by FTIR. All bands are assigned according to previous literature reports. 11,39-42 Specifically, the bands measured at 540, 730, 790, and 900 cm⁻¹ are all assigned to vibrational and stretching modes of the P-O-P bonding. The Q^n terminology is widely applied for explaining the degree of polymerization of phosphate glasses. 11,16,31,43 Here, n represents the number of bridging oxygens in the network. A higher n number represents a higher degree of polymerization of the glass network. The presence of Q1 species is indicated by the symmetric and asymmetric PO₃²⁻ stretching modes at 1000 and 1100 cm⁻¹. The weak signals at 900 and 1220 cm⁻¹ are assigned to the asymmetric P-O-P and PO₂⁻ vibrations, which indicates the presence of Q² units. However, the Q² signal is much weaker than Q¹ signal. The band around 3600 and 1600 cm⁻¹ is assigned to the symmetric stretching and the deformation modes of O-H groups, respectively, which can originate from surface hydroxyl groups or physically adsorbed surface water. The band at 2900 cm⁻¹ is assigned to C-H stretching modes associated with residual organics. Figure 3 shows the 31P MAS NMR data measured under quantitative conditions from CPPs, where each deconvoluted resonance is assigned according to previous literature values. 27,31,44 From Table 2, 75.3% of Q°, 24.3% of Q¹, and 0.4% of Q² species comprise the CPP structure, thus

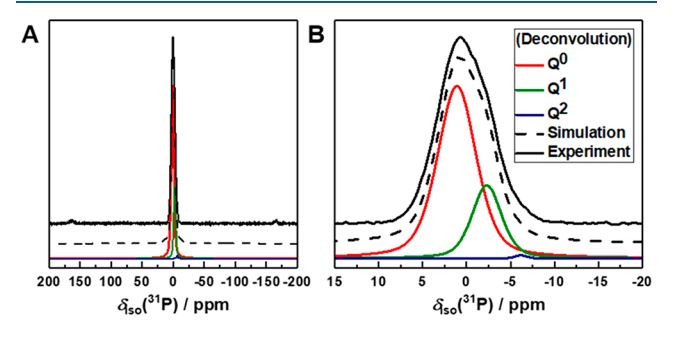


Figure 3. 31 P MAS NMR spectra of CPP-4 presented in the range of (A) -200-200 ppm and (B) -15-15 ppm. Predominant Q^0 and Q^1 species indicate a low degree of polymerization.

Table 2. ³¹P MAS NMR Peak Parameters of CPP-4

$\delta_{ m iso}$ (ppm)	Q^n	fwhm (ppm)	relative intensity (%)
1.1	Q^0	5.2	75.3
-2.3	Q^1	4.0	24.3
-6.2	Q^2	1.6	0.4

indicating a very low degree of polymerization throughout the phosphate network. Hence, the glass network is predominantly connected by P–O–Ca bonds rather than P–O–P bonds. The theoretical phosphate glass compositions sustaining pure Q° , Q^1 , and Q^2 speciation are $(P_2O_5)_{25}-(CaO)_{75}$, $(P_2O_5)_{33}-(CaO)_{67}$, and $(P_2O_5)_{50}-(CaO)_{50}$, respectively. Therefore, the theoretical composition of CPPs with 75.3% of Q° , 24.3% of Q^1 , and 0.4% of Q^2 species is close to $(P_2O_5)_{27.14}-(CaO)_{72.86}$ (calculated by weighted average). This NMR-derived composition is consistent with EDX and ICP-MS results of Table 1.

Effects of Electrospray Parameters on the Size. The first electrospray parameter studied is the flow rate of the sol solution. In the electrospray process, as the applied voltage increases, the spraying mode changes from dripping mode to spindle mode, and Taylor cone-jet mode. 45-47 Throughout this study, the Taylor cone-jet mode was applied because it generates relatively more monodispersed particles with predictable sizes. According to the scaling law, 35,48,49 the jet diameter is proportional to the flow rate and governs the size of as-generated droplets and particles. Our DLS and TEM results (Figure 4, SI Figure S1 and Table S1) are consistent with this prediction. As the flow rate increases from 0.05 (CPP-1, SI Table S1) to 0.4 (CPP-3, SI Table S1) mL/h, the mean diameter (Z-Ave.) of CPPs increases from 345.5 to 952.3 nm. The polydispersity index (PDI) remains around 0.25 for CPPs prepared from the flow rate of 0.05-0.2 mL/h. The PDI, however, increases significantly to 0.564 when the flow rate is 0.4 mL/h. The increasing polydispersity is due to a less stable Taylor-cone jet when the flow rate is larger than 0.4 mL/h. The other two parameters, emitter voltage (14.5–16.5 kV) and working distance (4-10 cm), however, do not result in a significant change of the particle size (Figure 4B,C). Note that a second peak \sim 5000 nm with 0.5-14% in intensity exists in all samples. This was attributed to larger particles formed due to the bursting spray caused by the occasional congestion of the nozzle. This bursting spray may also explain the relative polydisperse nature of as-prepared CPPs. More detailed size information (Z-Ave., PDI, peaks, peak percentage, and standard deviation for each peak) can be found in SI Table S1.

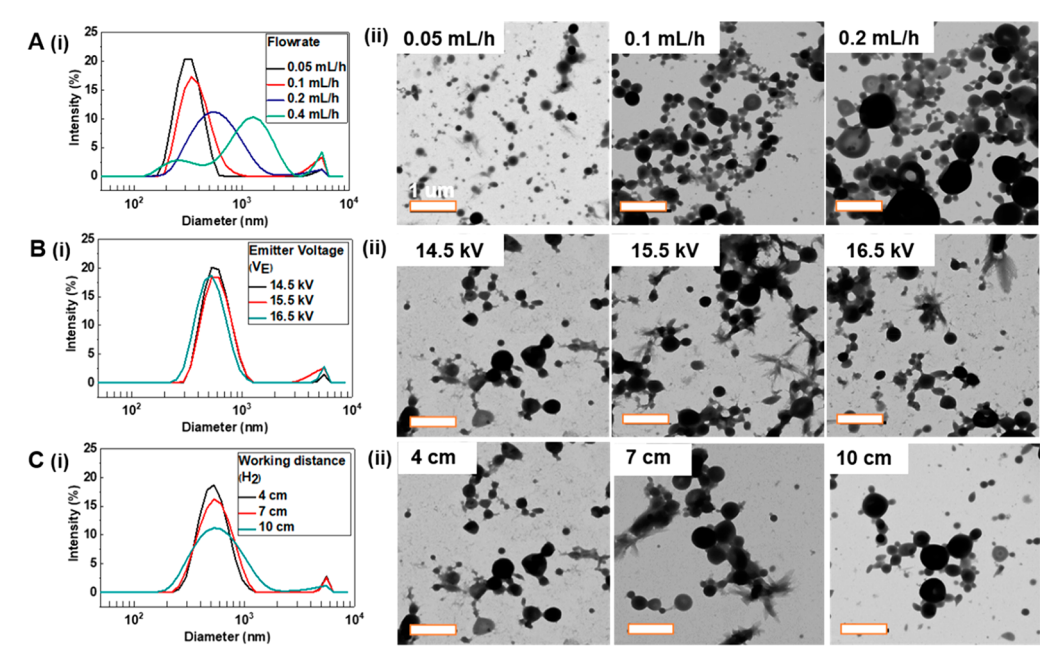


Figure 4. DLS and TEM images showing the effect of (A) flow rate, (B) emitter voltage, and (C) working distance on the size distribution of CPPs. The flow rate was adjusted from 0.05 (CPP-1) to 0.1 (CPP-2), 0.2 (CPP-4), and 0.4 (CPP-3) mL/h; the emitter voltage was adjusted from 14.5 (CPP-5) to 15.5 (CPP-6), and 16.5 (CPP-7) kV; the working distance was adjusted from 4 (CPP-5) to 7 (CPP-8), and 10 (CPP-4) cm. See SI Table S1 for details on synthetic parameters. See SI Figure S1 for the TEM image for CPP-3. The mean diameter of particles increases as the flow rate increases from 0.05 to 0.4 mL/h and does not vary significantly with the change of emitter voltage and working distance in the tested range. Scale bar, 1 μm.

Effects of the Solvent Mixture on the Morphology.

Both the size and morphology (or shape) have been known to greatly affect the cell internalization of synthetic particles. 50-54 It is therefore essential to be able to control the morphology of CPPs for potential biomedical applications. Electrospray not only shows flexibility in the control over the particle size but also the particle morphology. 27,35,55-66 One factor that influences the morphology of particles during electrospray is the evaporation behavior of solvents. For example, the preparation of porous particles with tunable pore structures 55,67,68 and nonspherical particles (e.g., red-blood celllike)⁶⁹ have been demonstrated via controlling the evaporation of solvents. We hypothesized that the addition of a highboiling point solvent to the sol solution can alter the solvent evaporation behavior and thus the morphology of CPPs. TBP was selected as a model additive because of its much higher boiling point relative to all other reactants in the sol solution (Table 3). Various amounts of TBP were added to the sol solution immediately before the electrospray. An interesting evolution of the morphology CPPs was observed with the increase of TBP addition (Figure 5B). Without adding TBP, the CPPs surface is highly wrinkled and resembles a carnation flower (Figure 5B (i)). As the added TBP increases from 4.3 to

Table 3. Comparison of the Boiling Point of Reactants

chemical	boiling point $({}^{\circ}C)^{a}$
n-butyl phosphate(Alfa Aesar)	~124
calcium methoxyethoxide (ABCR, 20% in methoxyethanol)	118
2-methoxyethanol(Sigma-Aldrich, 99.9%)	124-125
tributyl phosphate(Sigma-Aldrich, 99%)	289

^aData provided by corresponding manufacturers.

18.3 vol %, the surface becomes increasingly smooth, and the morphology changes from golf ball-like (Figure 5B (ii)) to mildly dented (Figure 5B (iii)), and then apple-like (Figure 5B (iv)). The increase of TBP concentration to 34.9 vol % can further reduce the surface dents and wrinkles (SI Figure S2). See SI Figure S3 for DLS results of CPPs prepared from various TBP concentrations.

The TBP does not participate in the chemical reactions because no significant compositional difference resulted from the TBP addition (Table 1). Therefore, the observed morphology evolution is more likely a result of changes in the physical properties of the sol caused by TBP addition. A possible mechanism is proposed and shown in Figure 5A. A higher amount of TBP addition will increase the overall boiling point of the solvent mixture meaning a slower evaporation rate. This reduced evaporation rate may allow for a more sufficient inward solute diffusion and homogeneous shrinkage of the liquid droplet before the formation of a solid crust. As a result, a smaller void-to-crust volume ratio is possible upon the complete evaporation of solvents. Therefore, the particle is more robust to resist the tendency toward structural collapse and result in more smooth and spherical particles. On the contrary, with less TBP, the solvent evaporation can be so fast that a crust forms in an early stage. After complete solvent evaporation, a larger void-to-crust volume ratio is possible. Such a relatively larger void volume will force the particle to have a higher degree of structural collapse and the formation of a more wrinkled surface. Of course, further studies are necessary to validate this hypothesis.

Hydro-Expansion and Degradation of CPPs. Bulk phosphate glasses have been known for their good biodegradability. Here, the dissolution behavior of CPPs of various morphologies (CPPs-4, -9, -10, and -11 shown in Figure 5) was investigated using an inverted optical micro-

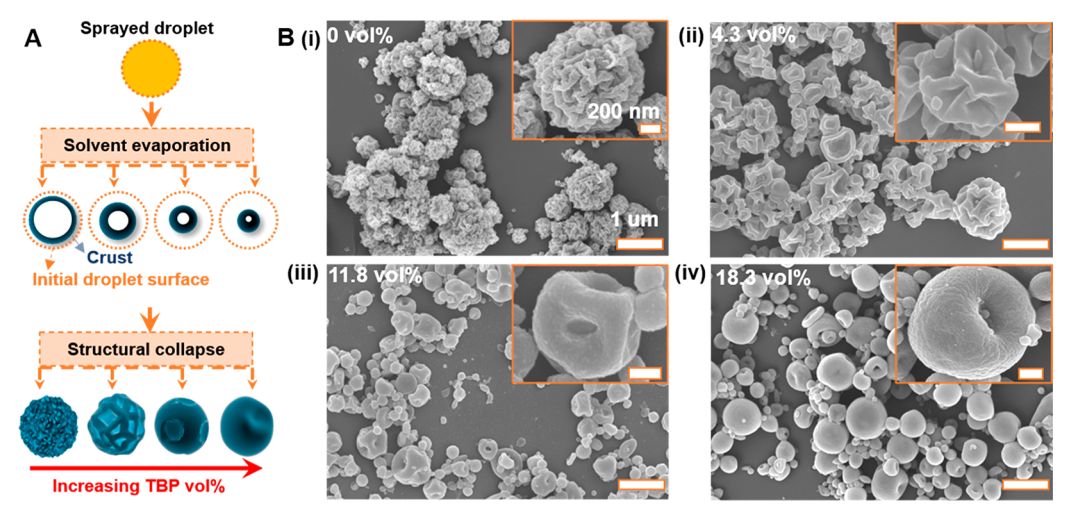


Figure 5. (A) Schematic illustration of a hypothesized mechanism for the evolution of the morphology of CPPs. A higher amount of TBP increases the boiling point of the solvent mixture, which will slow down the evaporation of the solvent and allow for a more sufficient inward solute diffusion and a homogeneous shrinkage of the droplet before the formation of a void crust. This more sufficient inward solute diffusion process can lead to a smaller void-to-crust volume ratio upon the complete solvent removal and a lower degree of structural collapse and, therefore, a smooth surface. (B) SEM images showing the evolution of the morphology of CPPs with the increase of tributyl phosphate (TBP) addition in the sol solution from (i) 0 vol % (carnation-like, CPP-9), (ii) 4.3 vol % (golf ball-like, CPP-10), (iii) 11.8 vol % (dented, CPP-11) to (iv) 18.3 vol % TBP (apple-like, CPP-4). The surface smoothness increases with the increase of TBP addition. Inset images: higher magnification images showing a representative particle for each case. Scale bar: 1um for all low-magnification images; 200 nm for all high-magnification images.

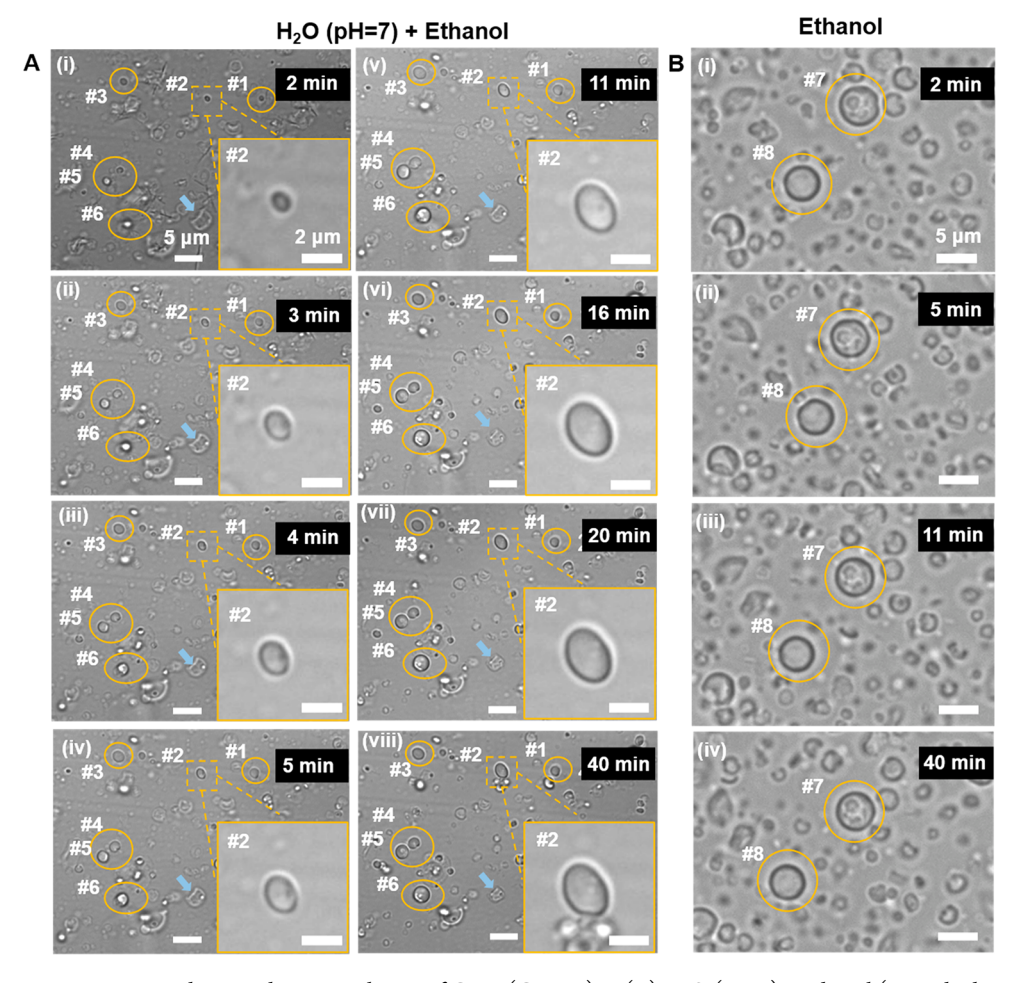


Figure 6. Optical microscopy images showing the size evolution of CPPs (CPPs-4) in (A) H_2O (pH 7) + ethanol (Inset: high magnification images of particle #2) and (B) pure ethanol over time. CPPs expansion was observed in in the presence of H_2O but not in pure ethanol. The light blue arrow indicates a particle that shrinks over time, which may be attributed to the existence of internal voids. Scale bar: 5 μ m for low magnification images and 2 μ m for high magnification images.

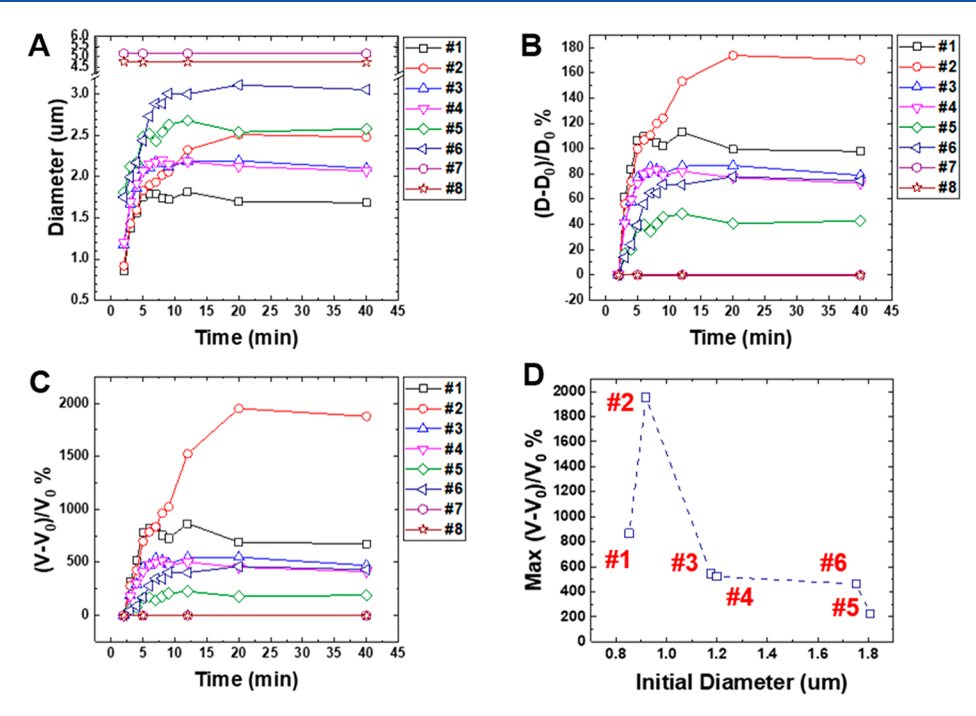


Figure 7. Quantification of the hydro-expansion of CPPs over time based on image analysis of optical microscopy images as shown in Figure 6. (A) Diameter versus time. (B) The change in relative diameter versus time. (C) Relative volume change versus time. (D) Maximum relative volume change versus initial diameter. For the calculation of relative diameter and volume changes, diameter and volume values at t=2 min were used as D_0 and V_0 and an ideal spherical shape was assumed. There was an initial burst increase of diameter within the first 5 min. The number-average of the maximum $(D-D_0)/D_0$ % and $(V-V_0)/V_0$ % is 95% and 720% respectively. The maximum relative volume change decreases with increasing initial particle size.

scope. Briefly, CPPs in ethanol solution were dropped to a 35 mm glass-bottom dish and then aqueous solutions of various pH (pH 5.2, 7, and 10) were added to the dish respectively to initiate the hydration. We then waited two minutes to allow particles to settle down and stabilize on the bottom of the dish. In the acidic condition (pH 5.2), CPPs dissolve instantly (within 10s) regardless of their morphologies, as evidenced by a significant volume shrinkage (SI Figures S4 (A), S5 (A), S6 (A), S7 (A). On the contrary, an interesting hydro-expansion behavior was observed for CPPs of all morphologies when they were hydrated at pH 7 (SI Figure S4 (B), S5 (B), S6 (B) and Figure 6) and pH 10 (Figure S4 (C), S5 (C), S6 (C), S7(C). Such dissolution/expansion behaviors were not observed in pure ethanol solution (Figure 6B), indicating that the dissolution/expansion of CPPs is associated with the interaction between CPPs and water. Note that some particles only shrank even when pH 7 (highlighted by the blue arrow, Figure 6) and pH 10 (SI Figure S4). This may be due to the void nature of some CPPs.

As an example of quantitative analysis, the average diameter of particles (CPPs-4) numbered in Figure 6 during the hydration process at pH 7 and pure ethanol was measured using Image-Pro Plus 6 software. The evolution of the diameter, relative diameter change ((D- D_0)/ D_0 %), and relative volume change (($V-V_0$)/ V_0 %) over time is shown in Figure 7. Figure 7A clearly shows that no size change occurred for CPPs in pure ethanol (#7 and #8). As for CPPs in the presence of neutral H₂O (#1-#7), an initial "burst" increase of diameter within the first 5 min was observed. After that, the diameter change reaches a plateau. The maximum relative diameter change varies from ~48% (particle #5, Figure 7B) to ~173% (particle #2, Figure 7B). Similarly, the relative volume change varies from ~230% (particle #5, Figure 7C) to ~1950%

(particle #2, Figure 7C). The number-weighted average values for the maximum $(D-D_0)/D_0$ % and $(V-V_0)/V_0$ % are 95% and 720%, respectively. The actual relative diameter change and volume change should be more than 95% and 720% because the diameter and volume at t = 2 min were used as initial values in our calculation. Figure 7D shows that the maximum relative volume change tends to decrease with the increase of the initial particle size. This could be a result of the difference in the surface-to-volume ratio of particles. The relative volume change of CPPs caused by the hydration is comparable with that of some polymer particles reported in the literature, for example, 330% for chitosan microparticles, 70 200% for P(St-co-DMAEMA) nanoparticles,⁷¹ 230% for PLGA microparticles,⁷² and 800% for gelatin nanoparticles.⁷³ SEM images of CPPs hydrated at pH 7 and then dried at 100 °C (SI Figure S8) shows that the hydration process significantly altered the morphology of CPPs. For example, the wrinkled surface of CPP-9 became smooth. In some cases (CPP-10 and CPP-4), steps/facets typically observed in crystal materials appeared. We hypothesize that the observed hydro-expansion behavior may be attributed to chemical reactions between water and CPPs to form new calcium phosphate phase (s) that has (have) a larger volume. A more systematic study combining microscopy, FTIR, TGA, and XRD will be carried out in the future to verify the actual mechanism for the hydro-expansion.

The degradation of bulk phosphate-based glasses is known to release component ions. To monitor the ion release of CPPs, a dynamic dissolution experiment was carried out by using a homemade flow cell design. This flow cell is configured from a syringe and syringe filter. It allows for the deposition of CPPs on a syringe filter membrane and a continuous flow of Millipore water passed through the membrane. The liquid samples were collected at the desired time points for ICP-MS

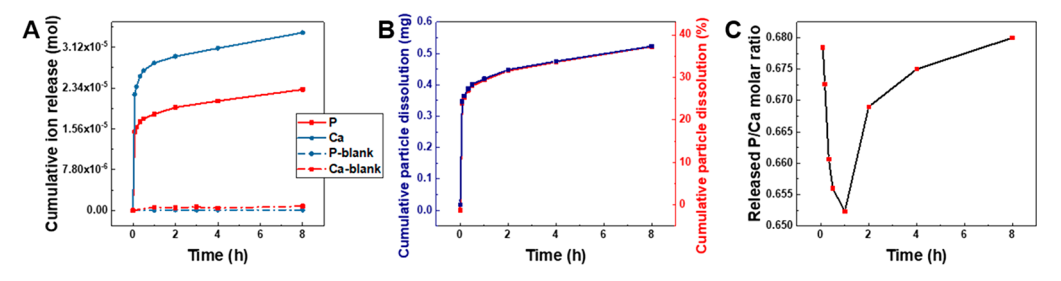


Figure 8. Dissolution of CPP-4 monitored with ICP-MS. (A) Cumulative ion release of P and Ca ions versus time showing an initial burst release of P and Ca ions in the first hour and a linear release starting from the second hour. P-blank and Ca-blank curves were created from DI water running through a flow cell without particles. (B) Cumulative particle dissolution in weight (blue) and weight percentage relative to initial particles (red) over time calculated based on cumulative ion release. (C) Released P/Ca molar ratio versus time. The released P/Ca molar ratio decreases in the first hour and then increases.

analysis. Figure 8A shows the cumulative release of P and Ca ions expressed as molar. The ion release curve of both P and Ca can be divided into a nonlinear region (t = 0-2 h) and a linear region (t = 2-8 h). The nonlinear region is featured with an initial burst release of ions, which is consistent with the observed initial burst increase of size (Figure 7). As a control experiment, Millipore water was running through a blank flow cell (without particles) and analyzed with ICP-MS (P-blank and Ca blank, Figure 8A). As expected, no ion release was observed in the control experiment indicating no measurement error caused by the contamination from the flow cell. The calculated cumulative particle dissolution (Figure 8B) shows that ~0.54 mg or 38% of the initial CPPs were dissolved after 8h. Interestingly, as shown in Figure 8C, the molar ratio of P/ Ca released to water decreases in the first hour of dissolution. It then increases between 1 h and 8 h. This subtle variance of P/Ca molar ratio over time may be attributed to the dissolution mechanism of CPPs. The dissolution of phosphate-based glasses can either be governed by the hydrolysis of the P-O bond of the P-O-P unit or the hydration of the Ca-O bond of the P-O-Ca unit. If the dissolution is governed by the hydrolysis of the P-O bond, each basic phosphate unit containing calcium will be released intactly. In other words, one will expect a constant P/Ca molar ratio detected from water over time. On the contrary, a changing P/ Ca molar ratio was observed, indicating that the hydration of the Ca-O bond of the P-O-Ca unit is a more likely mechanism for the dissolution of CPPs. This is consistent with findings from previous research: the rate of hydrolysis of P-O-P bonds is significantly slower than the rate of hydration of the entire phosphate anion⁷⁴ and, as a result, phosphate anions can be separated intactly from their accompanying metal cations.⁷⁵

Inspired by the surprising hydro-expansion property of CPPs, we propose to utilize CPPs to construct a nanosystem that can mechanically ablate tissue. We envision using the expansion of the particle to destroy cells. When coated with a protease-selective peptide, this approach could offer targeted ablation of malignant tissue. It could also be reused to restore blood flow in occluded vessels. These ideas will be investigated in future work.

CONCLUSION

The preparation of calcium phosphate micro/nano- particles, $(P_2O_5)_{25}$ - $(CaO)_{75}$, via the combined sol-gel and electrospray method was studied in detail. It was found that the flow rate has a significant effect on the size of CPPs, while the working distance and voltage of the emitter in the tested range do not.

We also found that the surface smoothness of CPPs was improved with increasing tributyl phosphate concentration in the sol solution. This knowledge enabled us to prepare CPPs with an average diameter in the range of 345 to 952 nm and various shapes including carnation flower, golf-ball, and applelike. Interestingly, a hydro-expansion behavior of CPPs in aqueous solutions of pH 7 and 10 was discovered with optical microscopy. Specifically, CPPs can have a more than 95% increase in diameter and a 720% increase in volume within the first 5-10 min of hydration in a neutral aqueous media. Such a hydro-expansion process is accompanied by a two-stage ion release of phosphorus and calcium. We envision using the expansion of the particle to destroy cells. When coated with a protease-selective peptide, this approach could offer targeted ablation of malignant tissue. It could also be reused to restore blood flow in occluded vessels. These ideas will be investigated in future work.

■ MATERIALS AND METHODS

Synthesis of CPPs. Synthesis of the Sol for Electrospray. The following chemicals were used without further purification: *n*-butyl phosphate (NBP, a mixture of mono-*n*-butyl and di-*n*-butyl, Alfa Aesar), calcium methoxyethoxide (CME, ABCR, 20% in methoxyethanol), 2-methoxyethanol (2-ME, Sigma-Aldrich, 99.9%), tributyl phosphate (TBP, Sigma-Aldrich, 99%). NBP was diluted by 2-ME in a molar ratio of 1:3 (NBP:2-ME) and magnetically stirred at 800 rpm for 10 min. This mixture was cooled in an ice-bath. CME was added to the solution dropwise via a syringe pump (16 mL/h) with the solution being magnetically stirred. Upon the completion of CME addition, the solution was brought to room temperature and magnetically stirred overnight. See SI Table S1 for specific reactant addition.

Electrospray. The setup for electrospray is shown in Figure 1A. A 16 G metal needle was used as the emitter, which was charged by a high-voltage generator. A metal ring with a diameter of 2.5 cm was inserted 0.5 cm below the emitter, which was also charged by a secondary high-voltage generator. Both the emitter and ring electrode shared the same ground electrode. The ground electrode was inserted below the silicone oil bath. The ring electrode inserted between the emitter and the ground electrode serves for modifying the spatial distribution of the electric field and confine the spray inside the space that is collectible by the silicone oil bath. A silicone oil bath maintained at 150 °C was used as the collection medium for particles. An appropriate amount of TBP was added to the sol from the previous step and vortexed for 10 s right before electrospray. Asprepared sol solution was fed to the emitter at various flow rates and electrosprayed by the applied voltage. Various combinations of TBP addition, flow rate, emitter voltage (V_E) , ring voltage (V_R) , and working distance (ring-to-ground electrode distance, H₂) were studied to determine their influences on the particle size and morphology. See SI Table S1 for specific parameters. The resulting particles were centrifuged at 5000 rpm, washed with acetone three times, and then dried at 180 $^{\circ}$ C for 2 h.

Characterization. *SEM, EDX, TEM, and DLS.* SEM images were acquired with Zeiss Sigma 500 operated at 5 kV with a 30- μ m aperture and 10 mm working distance. CPPs were drop-coated on a silicon substrate (Ted Pella Inc.) and sputter-coated with gold alloys before SEM. For EDX, CPPs without gold alloy coating were used and the voltage and aperture was 20 kV and 60 μ m, respectively. TEM images were acquired with a JEOL 1200 EX II operating at 80 kV. DLS measurements were carried out using Zetasizer (ZS90, Malvern Panalytical) with CPPs in 2-methoxyethanol solution.

XRD, FTIR, and Solid State ³¹P MAS NMR. Dried CPPs-4 powders were used for XRD, FTIR, and ³¹P MAS NMR characterization. XRD and FTIR spectra were acquired using Panalytical XRD and PerkinElmer FTIR. The solid state ³¹P MAS NMR data were measured at ambient temperature using a Varian InfinityPlus-300 spectrometer ($B_0 = 7.05$ T) operating at a Larmor frequency of 121.5 MHz. The experiments were performed using a Varian HX 3.2 mm MAS probe spinning at a MAS frequency of 20 kHz. Quantitative data were acquired with direct detection (single pulse) methods using a π /6 flip angle and a recycle delay of 400 s. The NMR data processing was carried out using ssNake while spectral deconvolution was undertaken using Origin. All spectra were referenced against the IUPAC recommended primary reference of 85% H₃PO₄ (δ _{iso} = 0.0 ppm) via a secondary reference of ammonia dihydrogen phosphate (ADP) (δ _{iso} = 0.99 ppm).

Hydro-Expansion Observation. The hydro-expansion of CPPs was observed using an inverted optical microscopy (Keyence). Here, 0.1 mL CPPs in ethanol solution (1 mg/mL) was dropped to a 35 mm glass-bottom dish with a 14 mm microwell no. 1.5 cover glass (Cellvis). Two mL aqueous solutions with pH 5.2, 7, and 10 were added to the dish respectively to initiate the hydration of particles. The first image was taken after 2 min of waiting time, when particles naturally settled down on the bottom of the dish and self-stabilized. Images of the same area were taken at various time points and then analyzed by Image-Pro Plus 6 to determine the diameter of particles. pH 5.2 solution was citrate buffer. pH 7 solution was Millipore water. pH 10 solution was pH 10 calibration buffer for pH meters (Thermo Scientific).

Biodegradation Monitoring. Biodegradation was monitored via ICP-MS (iCAP RQ, Thermo Scientific): 1.4 mg CPP-4 (SI Table S1) was deposited on a syringe filter with a pore size of 0.22 μ m (Millex-GP). CPP-4 was used because the smallest particles found in this sample were larger than the pore size (see Figure 4 A(i)). ICP-MS samples were prepared as stated below. Millipore water was continuously pumped (1.2 mL/h) through the particle-deposited syringe filter using a syringe pump at room temperature. The liquid phase was collected at various time points (0 min, 5 min, 10 min, 20 min, 30 min, 1 h, 2 h, 4 h, 8 h, 24 h). A 0.1 mL aliquot of each of these liquids was mixed with 0.571 mL 70% HNO₃ and left for overnight digestion. Subsequently, Millipore water was added to make a solution of 10 mL. The same process was repeated for a flow cell without particles to create negative controls. The release of P and Ca was measured with standard curves created in the range of 0-1000 ppb prepared from commercial phosphorus standard and calcium standard (TraceCERT). All samples and standards contain 4% HNO₃. Results were expressed as a cumulative ion release in mole versus time.

ASSOCIATED CONTENT

Supporting Information

The Supporting Information is available free of charge at https://pubs.acs.org/doi/10.1021/acsanm.1c00285.

Table of synthetic parameters, DLS, TEM images, SEM images, Optical microscopy images of the hydration process at pH 5.2, 7, and 10 (PDF)

AUTHOR INFORMATION

Corresponding Author

Jesse V. Jokerst — Materials Science and Engineering Program, Department of NanoEngineering, and Department of Radiology, University of California, San Diego, La Jolla, California 92093, United States; ⊙ orcid.org/0000-0003-2829-6408; Email: jjokerst@ucsd.edu

Authors

Tengyu He — Materials Science and Engineering Program, University of California, San Diego, La Jolla, California 92093, United States; orcid.org/0000-0002-6767-4849

David G. Bradley – Depertment of Physics, University of Warwick, Coventry CV4 7AL, U.K.

Jiajing Zhou − Department of NanoEngineering, University of California, San Diego, La Jolla, California 92093, United States; © orcid.org/0000-0001-5203-4737

Alec Jorns – Department of NanoEngineering, University of California, San Diego, La Jolla, California 92093, United States

Yash Mantri — Department of BioEngineering, University of California, San Diego, La Jolla, California 92093, United States

John V. Hanna – Depertment of Physics, University of Warwick, Coventry CV4 7AL, U.K.; ⊙ orcid.org/0000-0002-0644-3932

Complete contact information is available at: https://pubs.acs.org/10.1021/acsanm.1c00285

Notes

The authors declare no competing financial interest.

ACKNOWLEDGMENTS

We acknowledge the support from the NSF funding under award no. 1845683 and NIH funding under award P30 NS047101. JVH thanks the EPSRC and the University of Warwick for partial funding of the solid-state NMR infrastructure at Warwick, and acknowledges additional support for this infrastructure obtained through Birmingham Science City: Innovative Uses for Advanced Materials in the Modern World (West Midlands Centre for Advanced Materials Projects 1 and 2). This latter support was augmented by partial funding from Advantage West Midlands (AWM) and the European Regional Development Fund (ERDF).

REFERENCES

- (1) Ting, H.-K.; Page, S. J.; Poologasundarampillai, G.; Chen, S.; Yu, B.; Hanna, J. V.; Jones, J. R. Phosphate content affects structure and bioactivity of sol-gel silicate bioactive glasses. *International Journal of Applied Glass Science* **2017**, 8 (4), 372–382.
- (2) Abou Neel, E. A.; Knowles, J. C. Physical and biocompatibility studies of novel titanium dioxide doped phosphate-based glasses for bone tissue engineering applications. *J. Mater. Sci.: Mater. Med.* **2008**, 19 (1), 377–86.
- (3) Bitar, M.; Salih, V.; Mudera, V.; Knowles, J. C.; Lewis, M. P. Soluble phosphate glasses: in vitro studies using human cells of hard and soft tissue origin. *Biomaterials* **2004**, 25 (12), 2283–2292.
- (4) Gough, J. E.; Christian, P.; Scotchford, C. A.; Jones, I. A. Longterm craniofacial osteoblast culture on a sodium phosphate and a calcium/sodium phosphate glass. *J. Biomed. Mater. Res.* **2003**, *66A* (2), 233–240.
- (5) Ceci-Ginistrelli, E.; Pugliese, D.; Boetti, N. G.; Novajra, G.; Ambrosone, A.; Lousteau, J.; Vitale-Brovarone, C.; Abrate, S.; Milanese, D. Novel biocompatible and resorbable UV-transparent

- phosphate glass based optical fiber. Opt. Mater. Express 2016, 6 (6), 2040.
- (6) Ceci-Ginistrelli, E.; Pontremoli, C.; Pugliese, D.; Barbero, N.; Boetti, N. G.; Barolo, C.; Visentin, S.; Milanese, D. Drug release kinetics from biodegradable UV-transparent hollow calcium-phosphate glass fibers. *Mater. Lett.* **2017**, *191*, 116–118.
- (7) Farag, M. M.; El-Rashedi, A. M. I.; Rüssel, C. In vitro biocompatibility evaluation of canasite-calcium phosphate glass-ceramics. *J. Non-Cryst. Solids* **2018**, 488, 24–35.
- (8) Li, J.; Cai, S.; Xu, G.; Li, X.; Zhang, W.; Zhang, Z. In vitro biocompatibility study of calcium phosphate glass ceramic scaffolds with different trace element doping. *Mater. Sci. Eng., C* **2012**, 32 (2), 356–363.
- (9) McLaren, J. S.; Macri-Pellizzeri, L.; Hossain, K. M. Z.; Patel, U.; Grant, D. M.; Scammell, B. E.; Ahmed, I.; Sottile, V. Porous Phosphate-Based Glass Microspheres Show Biocompatibility, Tissue Infiltration, and Osteogenic Onset in an Ovine Bone Defect Model. ACS Appl. Mater. Interfaces 2019, 11 (17), 15436–15446.
- (10) Padilla, S.; Roman, J.; Sanchez-Salcedo, S.; Vallet-Regi, M. Hydroxyapatite/SiO(2)-CaO-P(2)O(5) glass materials: in vitro bioactivity and biocompatibility. *Acta Biomater.* **2006**, 2 (3), 331–42.
- (11) Pickup, D. M.; Guerry, P.; Moss, R. M.; Knowles, J. C.; Smith, M. E.; Newport, R. J. New sol-gel synthesis of a (CaO)0.3(Na2O)-0.2(P2O5)0.5 bioresorbable glass and its structural characterisation. *J. Mater. Chem.* **2007**, *17* (45), 4777.
- (12) Saravanapavan, P.; Jones, J. R.; Pryce, R. S.; Hench, L. L. Bioactivity of gel-glass powders in the CaO-SiO2 system: A comparison with ternary (CaO-P2P5-SiO2) and quaternary glasses (SiO2-CaO-P2O5-Na2O). *J. Biomed. Mater. Res.* **2003**, *66A* (1), 110–119.
- (13) Obata, A.; Jones, J. D. C.; Shinya, A.; Kasuga, T. Sintering and Crystallization of Phosphate Glasses by CO2-Laser Irradiation on Hydroxyapatite Ceramics. *Int. J. Appl. Ceram. Technol.* **2012**, 9 (3), 541–549.
- (14) Novajra, G.; Perdika, P.; Pisano, R.; Baino, F.; Jones, J. R.; Boccaccini, A. R.; Detsch, R.; Vitale-Brovarone, C. Tailoring of Bone Scaffold Properties Using Silicate/Phosphate Glass Mixtures Key Engineering Materials; Trans Tech Publ, 2015; pp 283–288.
- (15) Knowles, J. C. Phosphate based glasses for biomedical applications. J. Mater. Chem. 2003, 13 (10), 2395.
- (16) Abou Neel, E. A.; Pickup, D. M.; Valappil, S. P.; Newport, R. J.; Knowles, J. C. Bioactive functional materials: a perspective on phosphate-based glasses. *J. Mater. Chem.* **2009**, *19* (6), 690–701.
- (17) Kim, H. W.; Lee, E. J.; Jun, I. K.; Kim, H. E.; Knowles, J. C. Degradation and drug release of phosphate glass/polycaprolactone biological composites for hard-tissue regeneration. *J. Biomed. Mater. Res., Part B* **2005**, 75 (1), 34–41.
- (18) Pickup, D. M.; Newport, R. J.; Knowles, J. C. Sol-gel phosphate-based glass for drug delivery applications. *J. Biomater. Appl.* **2012**, *26* (5), 613–22.
- (19) Govindan, R.; Girija, E. K. Drug loaded phosphate glass/hydroxyapatite nanocomposite for orthopedic applications. *J. Mater. Chem. B* **2014**, 2 (33), 5468–5477.
- (20) Habraken, W. J.; Wolke, J. G.; Jansen, J. A. Ceramic composites as matrices and scaffolds for drug delivery in tissue engineering. *Adv. Drug Delivery Rev.* **2007**, *59* (4–5), 234–48.
- (21) Santos, E. M.; Radin, S.; Ducheyne, P. Sol-gel derived carrier for the controlled release of proteins. *Biomaterials* **1999**, *20* (18), 1695–700.
- (22) Domingues, Z. R.; Cortés, M. E.; Gomes, T. A.; Diniz, H. F.; Freitas, C. S.; Gomes, J. B.; Faria, A. M.; Sinisterra, R. D. Bioactive glass as a drug delivery system of tetracycline and tetracycline associated with beta-cyclodextrin. *Biomaterials* **2004**, 25 (2), 327–33.
- (23) Ziegler, J.; Mayr-Wohlfart, U.; Kessler, S.; Breitig, D.; Günther, K.-P. Adsorption and release properties of growth factors from biodegradable implants. *J. Biomed. Mater. Res.* **2002**, 59 (3), 422–428.
- (24) Kaehr, B.; Townson, J. L.; Kalinich, R. M.; Awad, Y. H.; Swartzentruber, B. S.; Dunphy, D. R.; Brinker, C. J. Cellular

I

- complexity captured in durable silica biocomposites. *Proc. Natl. Acad. Sci. U. S. A.* **2012**, *109* (43), 17336–17341.
- (25) Lou, Y.-R.; Kanninen, L.; Kaehr, B.; Townson, J. L.; Niklander, J.; Harjumäki, R.; Jeffrey Brinker, C.; Yliperttula, M. Silica bioreplication preserves three-dimensional spheroid structures of human pluripotent stem cells and HepG2 cells. *Sci. Rep.* **2015**, *5* (1), 13635.
- (26) Meyer, K. C.; Labriola, N. R.; Darling, E. M.; Kaehr, B. Shape-Preserved Transformation of Biological Cells into Synthetic Hydrogel Microparticles. *Advanced Biosystems* **2019**, 3 (4), 1800285.
- (27) Foroutan, F.; Jokerst, J. V.; Gambhir, S. S.; Vermesh, O.; Kim, H.-W.; Knowles, J. C. Sol-Gel Synthesis and Electrospraying of Biodegradable (P2O5)55-(CaO)30-(Na2O)15 Glass Nanospheres as a Transient Contrast Agent for Ultrasound Stem Cell Imaging. ACS Nano 2015, 9 (2), 1868–1877.
- (28) Gilchrist, T.; Glasby, M. A.; Healy, D. M.; Kelly, G.; Lenihan, D. V.; McDowall, K. L.; Miller, I. A.; Myles, L. M. In vitro nerve repair—in vivo. The reconstruction of peripheral nerves by entubulation with biodegradeable glass tubes—a preliminary report. *Br. J. Plast. Surg.* 1998, 51 (3), 231—7.
- (29) Toumba, K.; Curzon, M. Slow-release fluoride. *Caries Res.* **1993**, 27 (Suppl. 1), 43-46.
- (30) Carta, D.; Pickup, D. M.; Knowles, J. C.; Smith, M. E.; Newport, R. J. Sol-gel synthesis of the P2O5-CaO-Na2O-SiO2 system as a novel bioresorbable glass. *J. Mater. Chem.* **2005**, *15* (21), 2134.
- (31) Carta, D.; Knowles, J. C.; Smith, M. E.; Newport, R. J. Synthesis and structural characterization of P2O5-CaO-Na2O sol-gel materials. *J. Non-Cryst. Solids* **2007**, 353 (11–12), 1141–1149.
- (32) Foroutan, F.; Kyffin, B. A.; Abrahams, I.; Knowles, J. C.; Sogne, E.; Falqui, A.; Carta, D. Mesoporous Strontium-Doped Phosphate-Based Sol-Gel Glasses for Biomedical Applications. *Front. Chem.* **2020**, *8*, 249.
- (33) Owens, G. J.; Singh, R. K.; Foroutan, F.; Alqaysi, M.; Han, C.-M.; Mahapatra, C.; Kim, H.-W.; Knowles, J. C. Sol-gel based materials for biomedical applications. *Prog. Mater. Sci.* **2016**, *77*, 1–79.
- (34) Pickup, D. M.; Valappil, S. P.; Moss, R. M.; Twyman, H. L.; Guerry, P.; Smith, M. E.; Wilson, M.; Knowles, J. C.; Newport, R. J. Preparation, structural characterisation and antibacterial properties of Ga-doped sol-gel phosphate-based glass. *J. Mater. Sci.* **2009**, *44* (7), 1858–1867.
- (35) He, T.; Jokerst, J. V. Structured micro/nano materials synthesized via electrospray: a review. *Biomater. Sci.* **2020**, 8 (20), 5555–5573.
- (36) Gross, K.; Andersons, J.; Misevicius, M.; Švirksts, J. Traversing Phase Fields towards Nanosized Beta Tricalcium Phosphate. *Key Eng. Mater.* **2013**, 587, 97–100.
- (37) Dorozhkin, S. V. Amorphous calcium (ortho)phosphates. *Acta Biomater.* **2010**, *6* (12), 4457–4475.
- (38) Layrolle, P.; Lebugle, A. Characterization and reactivity of nanosized calcium phosphates prepared in anhydrous ethanol. *Chem. Mater.* **1994**, *6* (11), 1996–2004.
- (39) Baia, L.; Muresan, D.; Baia, M.; Popp, J.; Simon, S. Structural properties of silver nanoclusters-phosphate glass composites. *Vib. Spectrosc.* **2007**, 43 (2), 313–318.
- (40) Ilieva, D.; Jivov, B.; Bogachev, G.; Petkov, C.; Penkov, I.; Dimitriev, Y. Infrared and Raman spectra of Ga2O3-P2O5 glasses. *J. Non-Cryst. Solids* **2001**, 283 (1), 195–202.
- (41) Moustafa, Y. M.; El-Egili, K. Infrared spectra of sodium phosphate glasses. J. Non-Cryst. Solids 1998, 240 (1), 144–153.
- (42) Byun, J.-O.; Kim, B.-H.; Hong, K.-S.; Jung, H.-J.; Lee, S.-W.; Izyneev, A. A. Properties and structure of RO—Na2O—Al2O3—P2O5 (R = Mg, Ca, Sr, Ba) glasses. *J. Non-Cryst. Solids* **1995**, 190 (3), 288–295.
- (43) Neel, E. A. A.; Knowles, J. C. Biocompatibility and other properties of phosphate-based glasses for medical applications **2009**, 156–182.
- (44) Lee, I.-H.; Foroutan, F.; Lakhkar, N. J.; Gong, M.-S.; Knowles, J. C. Sol-gel synthesis and structural characterization of P2O5–CaO–Na2O glasses. *Physics and Chemistry of*

- Glasses European Journal of Glass Science and Technology Part B 2013, 54 (3), 115–120.
- (45) Cloupeau, M.; Prunet-Foch, B. Electrostatic spraying of liquids: Main functioning modes. *J. Electrost.* **1990**, 25 (2), 165–184.
- (46) Cloupeau, M.; Prunet-Foch, B. Electrohydrodynamic spraying functioning modes: a critical review. *J. Aerosol Sci.* **1994**, 25 (6), 1021–1036.
- (47) Zong, H. X.; Xia, X.; Liang, Y. R.; Dai, S. Y.; Alsaedi, A.; Hayat, T.; Kong, F. T.; Pan, J. H. Designing function-oriented artificial nanomaterials and membranes via electrospinning and electrospraying techniques. *Mater. Sci. Eng., C* **2018**, *92*, 1075–1091.
- (48) Zhou, J.; Gao, D.; Yao, D.; K. Leist, S.; Fei, Y. Mechanisms and modeling of electrohydrodynamic phenomena. *International Journal of Bioprinting* **2018**, *5* (1), 166.
- (49) GaÑÁN-Calvo, A. M. On the general scaling theory for electrospraying. *J. Fluid Mech.* **1999**, *507*, 203–212a.
- (50) Čejkova, J.; Stepanek, F. Compartmentalized and Internally Structured Particles for Drug Delivery A Review. *Curr. Pharm. Des.* **2013**, *19* (35), 6298–6314.
- (51) Balmert, S. C.; Little, S. R. Biomimetic delivery with micro- and nanoparticles. *Adv. Mater.* **2012**, *24* (28), 3757–78.
- (52) Champion, J. A.; Mitragotri, S. Role of target geometry in phagocytosis. *Proc. Natl. Acad. Sci. U. S. A.* **2006**, *103* (13), 4930–4934.
- (53) Champion, J. A.; Mitragotri, S. Shape induced inhibition of phagocytosis of polymer particles. *Pharm. Res.* **2009**, *26* (1), 244–9.
- (54) Muro, S.; Garnacho, C.; Champion, J. A.; Leferovich, J.; Gajewski, C.; Schuchman, E. H.; Mitragotri, S.; Muzykantov, V. R. Control of endothelial targeting and intracellular delivery of therapeutic enzymes by modulating the size and shape of ICAM-1-targeted carriers. *Mol. Ther.* **2008**, *16* (8), 1450–1458.
- (55) Chen, A. Z.; Yang, Y. M.; Wang, S. B.; Wang, G. Y.; Liu, Y. G.; Sun, Q. Q. Preparation of methotrexate-loaded, large, highly-porous PLLA microspheres by a high-voltage electrostatic antisolvent process. *J. Mater. Sci.: Mater. Med.* **2013**, 24 (8), 1917–1925.
- (56) Misra, A. C.; Bhaskar, S.; Clay, N.; Lahann, J. Multi-compartmental particles for combined imaging and siRNA delivery. *Adv. Mater.* **2012**, 24 (28), 3850–6.
- (57) Zhou, F. L.; Chirazi, A.; Gough, J. E.; Cristinacce, P. L. H.; Parker, G. J. M. Hollow Polycaprolactone Microspheres with/without a Single Surface Hole by Co-Electrospraying. *Langmuir* **2017**, 33 (46), 13262–13271.
- (58) Dwivedi, P.; Han, S. Y.; Mangrio, F.; Fan, R.; Dwivedi, M.; Zhu, Z. A.; Huang, F. S.; Wu, Q.; Khatik, R.; Cohn, D. E.; Si, T.; Hu, S. Y.; Sparreboom, A.; Xu, R. X. Engineered multifunctional biodegradable hybrid microparticles for paclitaxel delivery in cancer therapy. *Mater. Sci. Eng., C* 2019, 102, 113–123.
- (59) Zhang, C. C.; Yao, Z. C.; Ding, Q. P.; Choi, J. J.; Ahmad, Z.; Chang, M. W.; Li, J. S. Tri-Needle Coaxial Electrospray Engineering of Magnetic Polymer Yolk-Shell Particles Possessing Dual-Imaging Modality, Multiagent Compartments, and Trigger Release Potential. ACS Appl. Mater. Interfaces 2017, 9 (25), 21485–21495.
- (60) Doshi, N.; Zahr, A. S.; Bhaskar, S.; Lahann, J.; Mitragotri, S. Red blood cell-mimicking synthetic biomaterial particles. *Proc. Natl. Acad. Sci. U. S. A.* **2009**, *106* (51), 21495–9.
- (61) Li, D.; Marquez, M.; Xia, Y. N. Capturing electrified nanodroplets under Rayleigh instability by coupling electrospray with a sol-gel reaction. *Chem. Phys. Lett.* **2007**, 445 (4–6), 271–275.
- (62) Bhaskar, S.; Hitt, J.; Chang, S. W.; Lahann, J. Multi-compartmental microcylinders. *Angew. Chem., Int. Ed.* **2009**, 48 (25), 4589–93.
- (63) Sarkar, D.; Mondal, B.; Som, A.; Ravindran, S. J.; Jana, S. K.; Manju, C. K.; Pradeep, T. Holey MoS2 Nanosheets with Photocatalytic Metal Rich Edges by Ambient Electrospray Deposition for Solar Water Disinfection. *Global Challenges* **2018**, 2 (12), 1800052.
- (64) Jana, A.; Jana, S. K.; Sarkar, D.; Ahuja, T.; Basuri, P.; Mondal, B.; Bose, S.; Ghosh, J.; Pradeep, T. Electrospray deposition-induced ambient phase transition in copper sulphide nanostructures. *J. Mater. Chem. A* **2019**, *7* (11), 6387–6394.

- (65) Suhendi, A.; Nandiyanto, A. B. D.; Munir, M. M.; Ogi, T.; Gradon, L.; Okuyama, K. Self-Assembly of Colloidal Nanoparticles Inside Charged Droplets during Spray-Drying in the Fabrication of Nanostructured Particles. *Langmuir* **2013**, 29 (43), 13152–13161.
- (66) Liu, B. S.; Nakata, K.; Sakai, M.; Saito, H.; Ochiai, T.; Murakami, T.; Takagi, K.; Fujishima, A. Mesoporous TiO2 Core-Shell Spheres Composed of Nanocrystals with Exposed High-Energy Facets: Facile Synthesis and Formation Mechanism. *Langmuir* **2011**, 27 (13), 8500–8508.
- (67) Zhang, Q.; Liu, J.; Wang, X.; Li, M.; Yang, J. Controlling internal nanostructures of porous microspheres prepared via electrospraying. *Colloid Polym. Sci.* **2010**, 288 (14), 1385–1391.
- (68) Gao, J.; Li, W.; Wong, J. S.-P.; Hu, M.; Li, R. K. Y. Controllable morphology and wettability of polymer microspheres prepared by nonsolvent assisted electrospraying. *Polymer* **2014**, *55* (12), 2913–2920
- (69) Park, C. H.; Chung, N. O.; Lee, J. Monodisperse red blood cell-like particles via consolidation of charged droplets. *J. Colloid Interface Sci.* **2011**, *361* (2), 423–8.
- (70) Ju, X.; Wang, X.; Liu, Z.; Xie, R.; Wang, W.; Chu, L. Red-blood-cell-shaped chitosan microparticles prepared by electrospraying. *Particuology* **2017**, *30*, 151–157.
- (71) Hu, Y.; Wang, J.; Zhang, H.; Jiang, G.; Kan, C. Synthesis and characterization of monodispersed P(St-co-DMAEMA) nanoparticles as pH-sensitive drug delivery system. *Mater. Sci. Eng., C* **2014**, *45*, 1–7.
- (72) Gasmi, H.; Danede, F.; Siepmann, J.; Siepmann, F. Does PLGA microparticle swelling control drug release? New insight based on single particle swelling studies. *J. Controlled Release* **2015**, 213, 120–127.
- (73) Bajpai, A. K.; Choubey, J. Design of gelatin nanoparticles as swelling controlled delivery system for chloroquine phosphate. *J. Mater. Sci.: Mater. Med.* **2006**, *17* (4), 345–358.
- (74) Bunker, B. C.; Arnold, G. W.; Wilder, J. A. Phosphate glass dissolution in aqueous solutions. *J. Non-Cryst. Solids* **1984**, *64* (3), 291–316.
- (75) Sales, B. C.; Boatner, L. A.; Ramey, J. O. Chromatographic studies of the structures of amorphous phosphates: a review. *J. Non-Cryst. Solids* **2000**, 263–264, 155–166.
- (76) Kuwahata, Y.; Takehara, H.; Ichiki, T. Comprehensive study on electrospray deposition in the single Taylor cone-jet mode by changing the spatial electric potential using a ring-shaped ternary electrode. *AIP Adv.* **2020**, *10* (4), 045107.